Materials Property Profiles for Actively Cooled Panels: An Illustration for Scramjet Applications

N. VERMAAK, L. VALDEVIT, and A.G. EVANS

A scheme for identifying and visualizing the material properties that limit the performance of candidate materials for actively cooled aerospace propulsion components is presented and illustrated for combustor panels for Mach 7 hypersonic vehicles. The method provides a framework for exploring the nonlinear interactions between design and materials optimization. By probing the active constraints along the border of feasible design space, the limiting properties have been elucidated for a representative group of candidate materials. Property vectors that enhance design options have also been determined. For one of the promising candidate alloys (the Ni-based superalloy, INCONEL X-750), the possibilities of reclaiming design space and lowering optimal combustor panel weight by tailoring its strength properties are assessed.

DOI: 10.1007/s11661-008-9768-y

I. INTRODUCTION

VARIOUS aerospace propulsion systems require active cooling to contend with the combination of high combustion heat fluxes or aerodynamic heating. The requirement is particularly stringent for internal surfaces, where heat dissipation by radiation is not an option. One prototypical example is the combustor of scramjet vehicles cooled by hydrocarbon fuel (Figure 1). In such a structure, significant thermomechanical stresses arise. Withstanding these stresses at operating temperatures necessitates careful design. A viable solution must resist several failure modes: yielding or rupture due to (a) thermal stresses, (b) pressure or inertial stresses, (c) combined thermomechanical stresses, as well as (d) softening of the material, (e) coking of the coolant, and (f) excessive pressure drop in the cooling ducts. The challenge is to assure that none of the failure modes are active over the pertinent ranges of the coolant flow rate $\dot{V}_{\text{eff}}$ and of the heat-transfer coefficient between the combustion gas and the solid surface h_G (Figure 1). To address this multivariable nonlinear problem, a physical model with an optimization protocol has been developed[1,2] and illustrated for a rectangular scramjet combustor operating in a Mach 7 hypersonic vehicle (Figure 1). A synopsis is presented in Appendix I. Vehicle integration has been addressed by providing solutions for two limiting boundary conditions (Figure 2). Design I (Figure 2(a)) with periodic supports along the base experiences bending due to the pressure in the combustion chamber. Design II attaches a sandwich panel with sufficient stiffness to prevent bending (Figure 2(b)).

The merit of such a code is that it facilitates communication between design variables and material properties. Namely, it provides a basis for selecting preferred materials and identifying directions for the development of advanced materials capable of providing superior performance at lower weight. The capabilities are exemplified by performance maps (Figure 3) and charts (Figure 4). The maps (Figure 3) identify the domains in which the material can function without failure, both with and without a (yttria-stabilized zirconia) thermal barrier coating (TBC).[3] The normalized versions of the coordinates used in the figures (flow rate ϕ and heat-transfer coefficient χ) provide greater insight into the thermal parameters than absolute values.[1] They can be interpreted as follows. The normalized flow rate is unity $\phi = 1$ when all of the fuel needed for stoichiometric combustion is used for combustor cooling. Larger values imply that excess fuel is needed just for cooling and smaller values that some of the fuel is used for cooling other parts of the vehicle. The normalized heat-transfer coefficient is unity $\chi = 1$ when the combustor is operating at steady state, without hot spots from shock waves. Larger values allow for the possibility of hot spots.

The preferred materials are those that combine the capability for performing at low flow rates and high heat transfer, and thereby enable functionality as close as possible to the upper left corner of the maps.[4] Each map is the result of two independent optimizations. One is performed absent a coating, because when such solutions exist they are preferred. When solutions only exist with a coating the optimization is conducted using the TBC thickness as a variable. The charts (Figure 4) reveal complementary information. They indicate the minimum mass of combustor panels able to satisfy the performance requirements for fixed χ but variable ϕ. The results, presented at two different levels of heat

N. VERMAAK, Doctoral Candidate, Materials Department, and A.G. EVANS, Professor, Materials and Mechanical Engineering Departments, are with the University of California, Santa Barbara, CA 93106-5050. Contact e-mail: natasha@engineering.ucsb.edu L. VALDEVIT, Assistant Professor, is with the Mechanical and Aerospace Engineering Department and Chemical Engineering and Materials Science Department, University of California, Irvine, CA 92697-3975.

Manuscript submitted July 22, 2008.
Article published online February 5, 2009

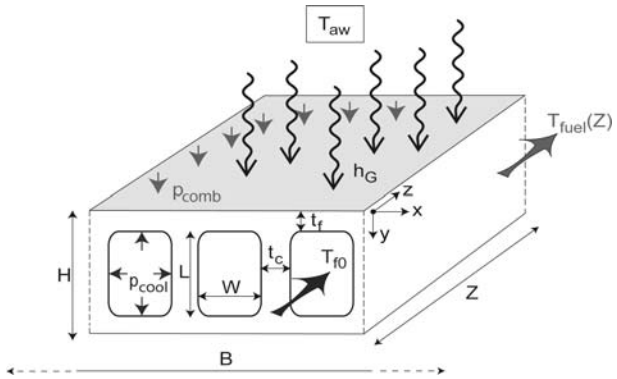

Fig. 1—Schematic of an actively cooled hypersonic combustor panel with thermostructural loads. The geometric coordinates are x, y, and z. Overall panel dimensions are length Z, width B, and thickness H. Mechanical loads are comprised of the combustion pressure p_{comb} and the coolant pressure p_{cool}. Thermal load is convective and described by the adiabatic wall temperature T_{aw} and the combustion heat-transfer coefficient h_G.

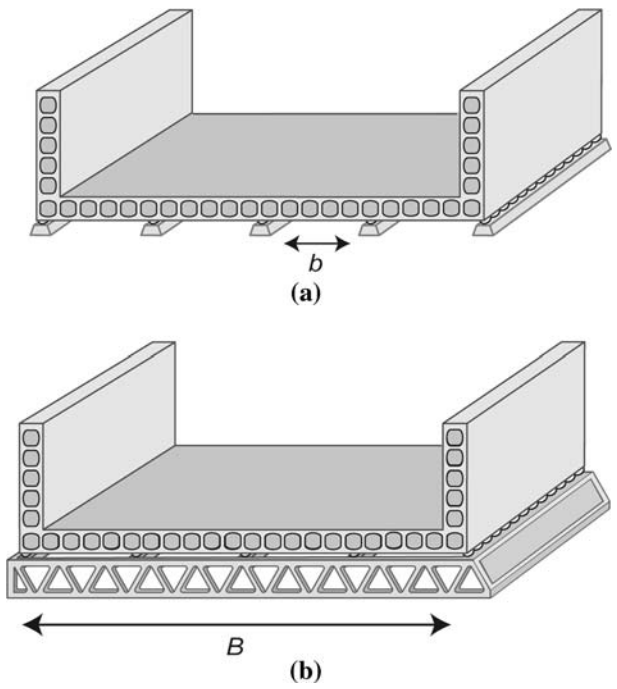

Fig. 2—Mechanical boundary conditions. (*a*) Design I uses periodic supports on rollers along the base of the panel. It allows bending between the supports due to the pressure in the combustion chamber. Support spacing is indicated by b and combustor width is B. (*b*) Design II attaches a sandwich panel with sufficient stiffness to prevent significant bending and thereby becomes insensitive to the combustion pressure.

transfer ($\chi = 1, 2$), reveal the following. When required to sustain larger χ, the panel is substantially heavier and the feasibility range in coolant flow ϕ is diminished. The panel weights for design II are appreciably lower than for design I (note the scale change on the figure). The superposition of a TBC has little effect on the weight except for design I at the higher χ, wherein a solution only exists when a TBC is used. Note that this information can be re-expressed through contours of

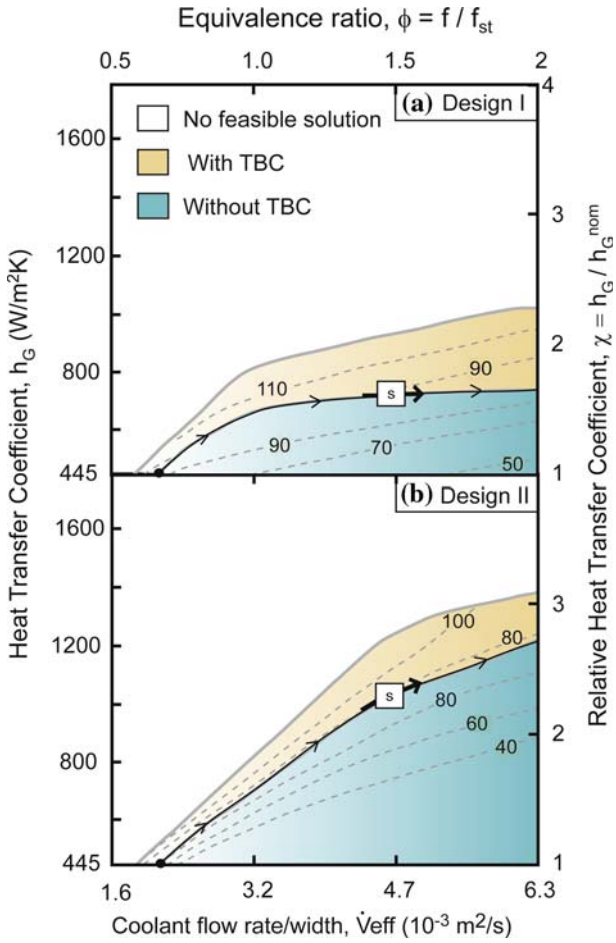

Fig. 3—(*a*) Design I and (*b*) Design II performance maps for INCONEL X-750, presented in $h_G(\dot{V}_{eff})$and $\chi(\phi)$ space. Normalizing parameters for the equivalence ratio ($\phi = f/f_{st}$) and the heat-transfer coefficient ($\chi = h_G/h_G^{nom}$) are those expected for steady-state Mach 7 flight conditions. Contours of mass (kg) are shown for regions with (tan) and without (blue) a TBC. Areas with no feasible solution are represented in white. Border of feasible design space is highlighted by trajectory *s*.

minimum weight superimposed onto the performance maps (Figure 3).

While displaying the information in this way reveals the material capability based on mass and robustness, it also conceals much of the insightful information contained within the output of the code. The most important omissions are the active constraints that limit the performance and dictate the minimum weight. Namely, it is not evident from Figures 3 or 4 whether it would be prudent to focus materials development on extending the highest temperature capability of a material or elevating the strength at intermediate temperature. This limitation is addressed in the present article.

The objective is to devise a scheme for identifying and visualizing activity constraints that can be used to direct materials development onto a pathway that maximizes the design options. In a first step, constraints that limit the performance of candidate materials are identified (Table I). Thereafter, the possibility of reclaiming design space by tailoring material properties is illustrated.

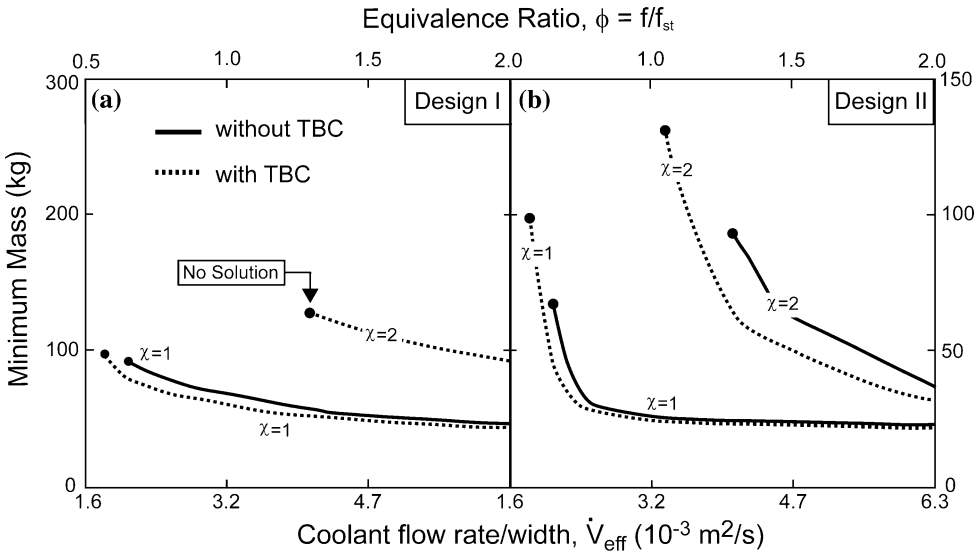

Fig. 4—Weight-performance charts that display minimum panel mass as a function of coolant flow rate for INCONEL X-750 both with and without a TBC (Table I). Results are for Designs I and II with fixed levels of heat transfer $\chi = 1$ and $\chi = 2$. Note the difference in scale between designs.

For this purpose, a Ni-based superalloy (INCONEL* X-750) is used as a benchmark material. This material is chosen for its availability, its well-understood intermediate and high temperature behavior,[5,6] and because it already shows considerable promise for postforming strengthening treatments.[7]

*INCONEL is a trademark of The Special Metals Corporation Group of Companies, Huntington, WV.

II. PERFORMANCE MAPS AND CHARTS

The code summarized in Appendix I[1] has been used to generate performance maps for a representative group of candidate materials (Table I, II) (Figure 5). The maps are ordered from the most to the least viable. The corresponding weight charts are presented in Figure 6 for two levels of heat transfer; one at steady state ($\chi = 1$) and the other for a high heat-transfer excursion ($\chi = 2$). The following features emerge. (1) For design I, among the candidates pursued, the Nb, Ni, and Cu alloys have the largest (comparable) admissibility domains, while the Ti alloy ($\beta 21S$) has the smallest despite its high specific strength.[8] The viability of the Nb alloy is subject to the availability of oxidation protection coatings.[9,10] (2) The C-SiC functions only at low heat flux. (3) The use of a TBC is generally effective at reclaiming design space. (4) Design II substantially increases the feasibility domain for all of the alloys, except for Ti. It is especially beneficial for C-SiC, which now occupies the same design space as the alloys.

The weight charts (Figure 6) provide a ranking. When viable, C-SiC always has the lowest weight, but it is not a feasible choice for design I at the higher heat transfer. Among the metallics, for most cases, the Ni or Nb alloys are the preferred candidates, albeit often at more than three times the weight of C-SiC. The exception is for design II at the higher heat transfer when the Cu alloy becomes weight competitive.

The reasons for these rankings can only be elucidated by examining the activity levels for the constraints and then probing into the most active. The concepts are developed in the subsequent sections.

III. ACTIVE CONSTRAINTS

A nondimensional activity index $\prod$ is defined for each of the imposed constraints (Appendix II, Table III). A

Table I. Candidate Materials and Their Thermomechanical Properties

Material	T^* (K)	$\sigma_{yield,ult}(T^*)$ (MPa)	$d\sigma_{yield}/dT^{(i)}$ (MPa/K)	E (GPa)	CTE (ppm/K)	k_s (W/mK)	ρ_s (kg/m^3)
INCONEL X-750	1100*	527	−0.4	130	16.0	23	8276
Ti β 21S	815	617	−1.5	100	10.3	21	4940
C-103	1365	138	−0.1	85	7.0	35	8860
GrCop-84	970	100	−0.2	90	19.0	285	8756
C-SiC	1810	200	—	100	2.0	15 (‖), 5(⊥)	2000
TBC (ZrO_2)	—	—	—	—	—	1	3000

*Aggressive T^* values were chosen for the candidate materials.

Table II. Thermophysical Properties of Hydrocarbon Jet Fuel

Fuel	k_f (W/mK)	μ_f (Pa·s)	$c_{p,f}$ (J/kg·K)	Pr_f	ρ_f (kg/m^3)	T_{coke} (K)
JP-7*	0.11	1.984×10^{-4}	2575	4.64	800	975

*Generalized properties of hydrocarbon jet fuels are used to approximate JP-7.

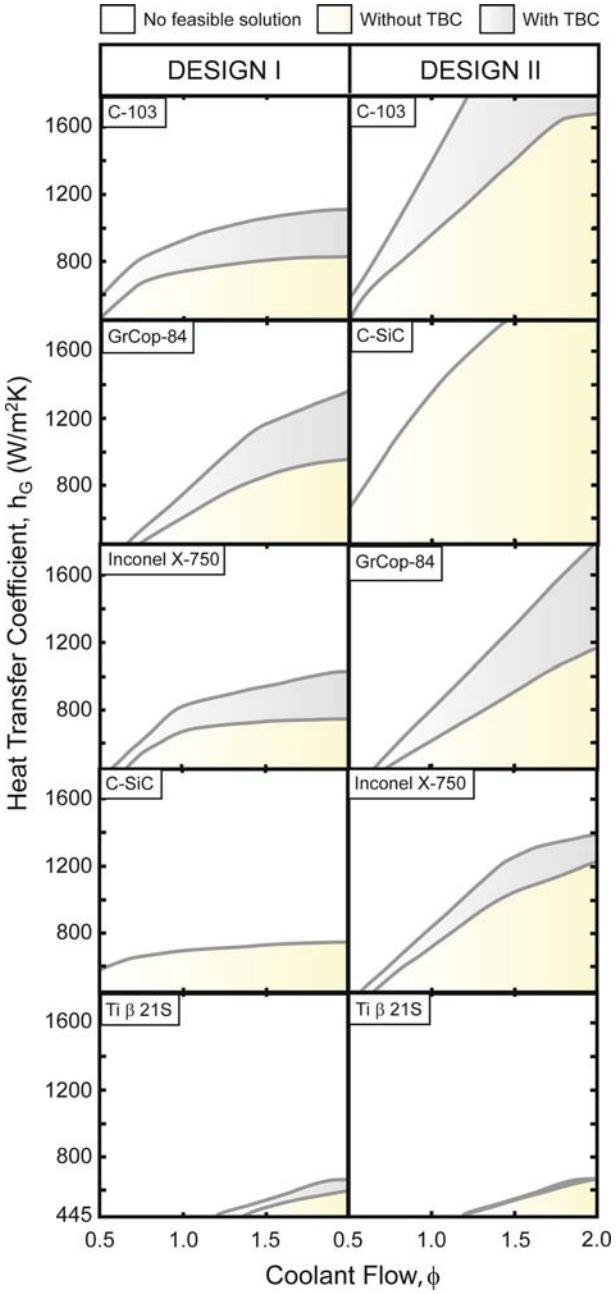

Fig. 5—(*a*) Design I and (*b*) Design II performance maps for a number of candidate materials (Table I), presented in $h_G(\phi)$ space. Normalizing parameter for the equivalence ratio ($\phi = f/f_{st}$) is that expected for steady-state Mach 7 flight conditions. Each map is the result of two independent optimizations. One (yellow) is performed absent a coating because when such solutions exist, they are preferred. When solutions exist only with a coating (light gray), the optimization is conducted using the TBC thickness as a variable. Areas without a feasible solution are in white. The maps are ordered from the most to the least viable.

constraint is active when this index reaches unity; when smaller, it has no effect on the optimum geometry. The constraints can be classified into three groups. Groups I and II are physically based; one embodying the resistance of the panel under the applied thermal and mechanical loads, and the other relating to system-imposed conditions (coolant temperature and pressure drop). Group III incorporates the manufacturing constraints on the minimum or maximum dimensions of the unit cell. The most illuminating trends are those along the border of the feasible design space, illustrated by trajectory *s* in Figure 3. The lower bound for the activity indices is constraint-specific, precluding comparison of inactive constraints in a global sense. However, in general, the closer a constraint is to unity the higher the likelihood that it will become active in an aggressive thermomechanical environment. Plots of $\Pi(s)$ that illustrate the methodology are presented on Figure 7. Because of the richness of the information, for clarity, the plots are presented only for the alloys in design I without a TBC. Note that only activity levels $\Pi \geq 0.6$ are of practical interest.

The nonlinearity of the optimization precludes straightforward analytical evaluation of the effect of each constraint. Nevertheless, some generalities emerge upon examining the constraints and the dependencies on geometry. Most fundamentally, because the panel comprises an obstacle between the combustion flux and the advecting coolant, left unconstrained the optimal thicknesses would go to zero. Therefore, to ensure a manufacturable design, minimum gages must be imposed. Thereafter, the following principles influence the dimensions selected by the optimization. (a) The minimum weight is achieved by augmenting the core member spacing and decreasing the member thicknesses. (b) Because the panel is subject to internal pressure loads, the deformation resistance of the faces is enhanced by reducing the core-member spacing and increasing the face thickness. (c) Since the coolant heat-transfer coefficient scales inversely with the hydraulic diameter, decreasing the core spacing and duct height is beneficial from a thermal standpoint. The conflicting requirements of points (a) through (c) result in the optimum. It is also possible to enhance the coolant heat transfer by modulating the duct internal surfaces,[11,12] but because this option is not considered, the code remains conservative.

Inspection of Figure 7 reveals the materials-specific challenge of reclaiming design space. That is, each material presents an individual challenge with a unique set of constraints limiting performance. Nevertheless, the following general characteristics emerge. Those based on dimensions are almost always active, invariably accompanied by at least one physical constraint.

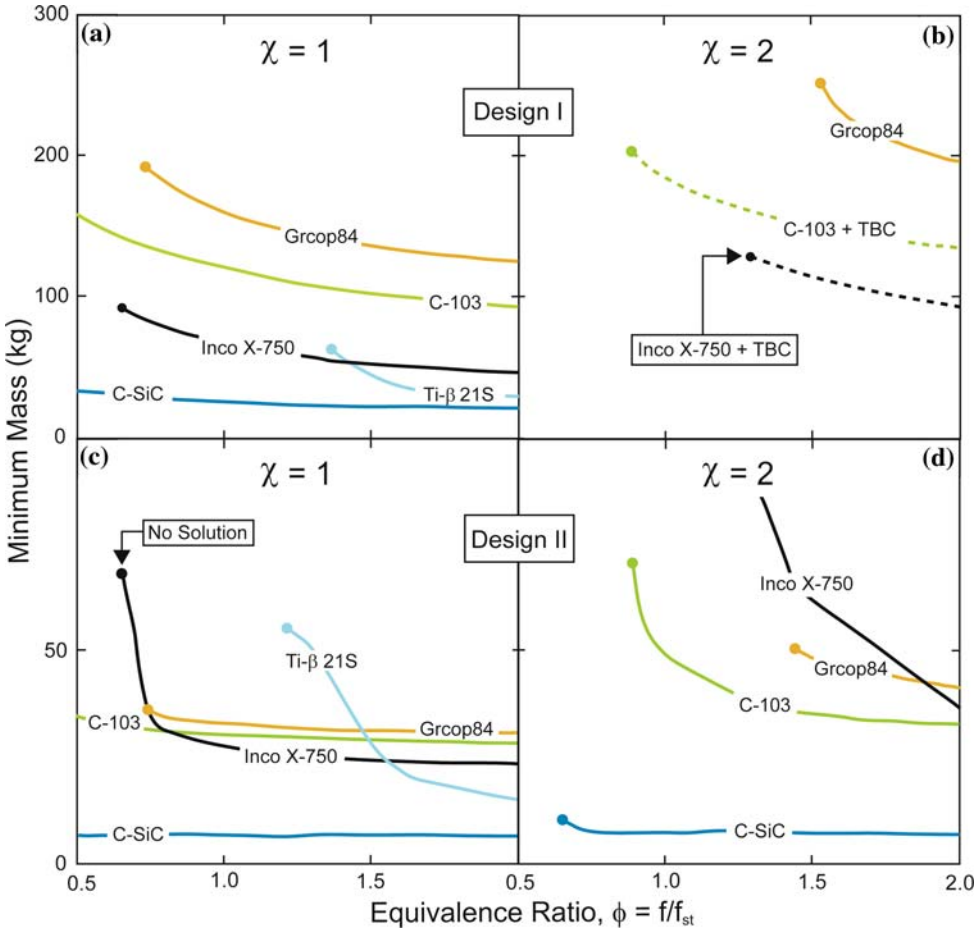

Fig. 6—Weight-performance charts that display minimum panel mass as a function of coolant flow rate for a number of material candidates (Table I). Results at representative levels of combustion heat transfer ($\chi = 1$ and $\chi = 2$) are presented for both design conditions. Note the difference in scale between designs. Solutions with a TBC are only shown if the material cannot survive without it.

Table III. Constraint Activity Indices and Associated Limiting Parameters

Constraint	Activity Index	Limiting Parameters
Net thermomechanical stresses	$\Pi^{(1)} = \max\left\{\frac{\sigma^{(i)}_{VM,\text{comb}}}{\sigma_{\text{yield}}(T^{(i)})}\right\}$	—
Mechanical stresses	$\Pi^{(2)} = \max\left\{\frac{\sigma^{(i)}_{VM,\text{mech}}}{\sigma_{\text{yield}}(T^{(i)})}\right\}$	—
Thermal stresses	$\Pi^{(3)} = \max\left\{\frac{\sigma^{(i)}_{VM,\text{therm}}}{\sigma_{\text{yield}}(T^{(i)})}\right\}$	—
Fuel coking	$\Pi^{(4)} = \frac{T^{\max}_{\text{fuel}}}{T_{\text{coke}}}$	$T^0_f = 400\text{K};\ T_{\text{coke}} = 975\ \text{K}$
Material softening	$\Pi^{(5)} = \frac{T^{\max}_{\text{solid}}}{T^*}$	$T^0_f = 400\text{K}$; T^* (Table I)
Pressure drop	$\Pi^{(6)} = \frac{\Delta p}{\Delta p^c}$	$\Delta p^c = 0.1\ \text{MPa}$
TBC thickness	$\Pi^{(7)} = \frac{t_{\text{TBC}}}{t^{\max}_{\text{TBC}}}$	$t^{\max}_{\text{TBC}} = \min\{0.25t_f, 0.3\,\text{mm}\}$
Minimum channel height, L	$\Pi^{(8)} = \frac{L_{\min}}{L}$	$L_{\max} = 20.0\,\text{mm}; L_{\min} = 5.0\,\text{mm}$
Minimum channel width, W	$\Pi^{(9)} = \frac{W_{\min}}{W}$	$W_{\max} = 40.0\,\text{mm}; W_{\min} = 2.0\,\text{mm}$
Minimum gage, t_f	$\Pi^{(10)} = \frac{t_{f,\min}}{t_f}$	$t_{f,\max} = 5.0\,\text{mm}; t_{f,\min} = 0.4\,\text{mm}$
Minimum gage, t_c	$\Pi^{(11)} = \frac{t_{c,\min}}{t_c}$	$t_{c,\max} = 5.0\,\text{mm}; t_{c,\min} = 0.4\,\text{mm}$

Moreover, some are active over a majority of the feasibility border s while others become active only at one of the extremes of the design map (namely, at low coolant flow or high heat transfer). Among the geometric constraints, the minimum channel height L is always active, while the maximum core thickness t_c and

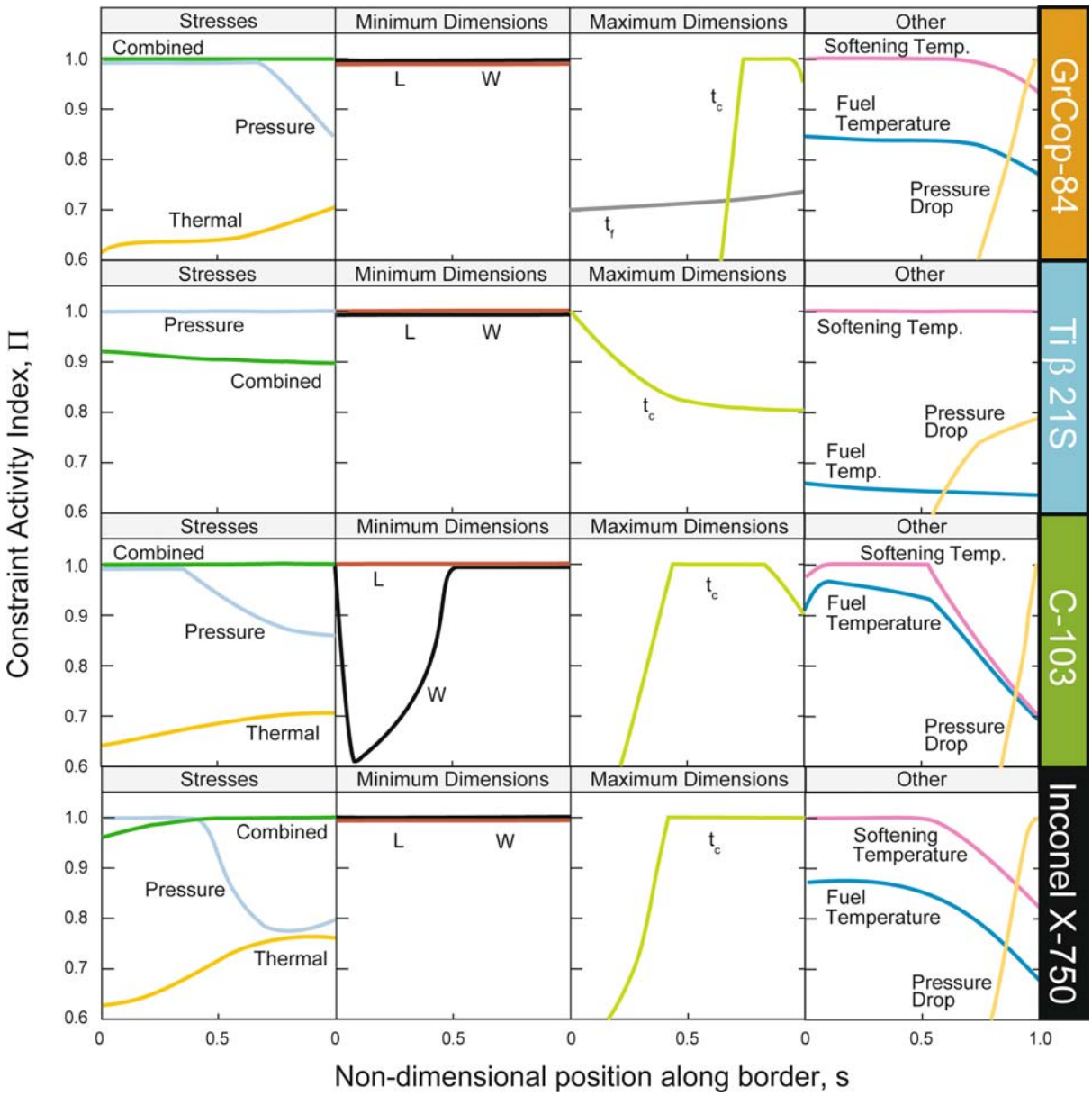

Fig. 7—Constraint activity maps for candidate materials without a TBC using Design I. The constraint activity index is presented in the coordinates Π (*s*) where *s* is the nondimensional feasibility border for each material, an example of which is shown in Figure 3. Recall that the code provides an activity index Π ≤ 1.0, where unity designates that the constraint is active. All values less than unity designate an inactive constraint. For convenience, only activity levels in the range 0.6 ≤ Π ≤ 1 are plotted.

minimum channel width *W* are active in most circumstances. These dimensions reach their minimum or maximum allowable in order to limit the stresses and temperatures in the hot face. The constraint on softening temperature is almost always active toward the extreme of low coolant flow, while the constraint on the maximum pressure drop typically approaches unity toward the high coolant flow extreme.

IV. MATERIALS ASSESSMENT

The basic features elucidated from the activity indices are illustrated for a Ni-based superalloy. Thereafter, the differences that arise among the other candidate materials are highlighted. For clarity of presentation, the assessment is conducted only for design I without a TBC. The effects of a design change or of the addition of a TBC can be explored using the same methodology.

A. *Ni-alloy INCONEL X-750*

The activities that approach unity along most of the feasibility border are as follows: (a) the stresses induced by the pressure or the combined thermal/pressure loads, (b) the minimum channel dimensions and maximum core member thickness, and (c) the softening temperature T^*. Increasing core member thickness is thermally

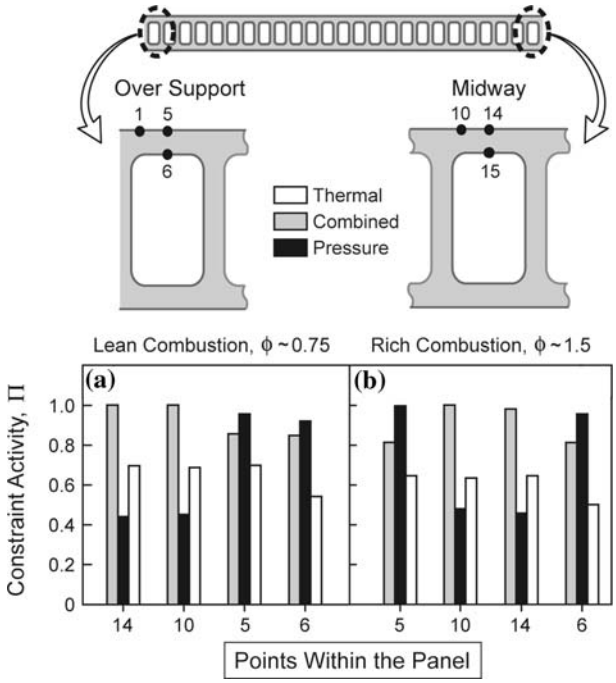

Fig. 8—Locations in the panel with the most active stress-induced constraints are highlighted in (*a* and *b*). The relative level of activity for (*b*) rich and (*a*) lean combustion scenarios in Design I is presented. All results refer to an INCONEL X-750 panel with fixed combustion heat transfer $\chi = 1$.

beneficial because the coolant heat-transfer coefficient scales inversely both with the hydraulic diameter and the number of ducts. The material becomes yield strength limited when large coolant flows are allowed, whereupon the combined thermal/pressure stresses are active. Some details are probed by examining four locations where the stress-based activities are closest to unity (Figures 8(a) and (b)). Results are presented at fixed heat transfer for lean ($\phi = 0.75$) and rich ($\phi = 1.5$) combustion scenarios. Two different channel locations must be examined; one over the supports and another midway (top of Figure 8). Both are equivalent thermally but differ mechanically because the bending due to combustion pressure induces tension in the hot face over the support but compression at the middle (Appendix II, Figure A3). These different pressure-induced components can interact with the thermal stresses to cause the two independent modes to be active simultaneously (Figure 8(b)). Over the supports, for low flow rates, locations 5 and 6 have activities closest to unity. At these locations, the stresses caused by the combustion pressure and panel-level-thermal gradients have opposite sign (Appendix II, Figure A3), with the former being most active. Namely, at these locations the individual stresses exceed the combined stresses. Conversely, midway at locations 10 and 14 the stresses have the same sign (Appendix II, Figure A3), causing the combined stresses to be most active (Figure 8(a)). At higher flow rates, the cooling capability increases, allowing t_c to reach its minimum and the core spacing to increase (Table IV). This dimensional change enhances the role of pressure-induced stresses and causes location 5 to replace location 14 as most active (Figure 8(b)). Location 10 remains active, partially because it is the only location where all contributions to stress have the same sign (Appendix II, Figure A3).

Table IV. Design I Optimal Geometries Associated With Figure 8

h_G (W/m^2 K)	ϕ	L (mm)	W (mm)	t_f (mm)	t_c (mm)
445	0.75	5.0	2.0	0.98	1.2
445	1.5	5.0	2.4	0.84	0.4

B. *Cu-Based Alloy GrCop-84*

The same activities approach unity for this alloy except for the maximum core member thickness (unity only in the region of highest heat transfer). More importantly, the face-sheet member t_f is much thicker. Evidently, the Cu-based alloy requires a much bulkier structure to withstand the same thermomechanical environment. That is, although its conductivity exceeds that for INCONEL X-750 by over an order of magnitude and its T^* is only about 10 pct lower, its strength at T^* is much lower (80 pct) requiring more material to support the stresses.

C. *Ti-Based Alloy Ti β 21S*

This alloy is limited along the entire feasibility border by its low softening temperature as well as the pressure-induced stresses. One avenue to reduce these stresses would be to reduce the channel aspect ratio and thicken the faces. However, face thickening increases the maximum solid temperature and compromises the softening temperature constraint.

D. *Nb-Based Refractory Alloy C-103*

This alloy exhibits unexpected similarities with INCONEL X-750 despite the vastly different individual properties (Table I). The only difference in constraint is that $\prod$ for the channel width becomes inactive over most of the range. This outcome highlights the nonintuitive nature of the optimization caused by the nonlinearities.

V. MATERIALS DEVELOPMENT OPPORTUNITIES

The code provides another, previously unexplored, capability. It enables the identification of material property pathways having the largest influence on design space reclamation. To illustrate the potential, we commence with a promising material candidate and assess the benefits of property enhancement vectors. Based on the preceding assessment, both the material softening temperature T^* and the material strength are critical limiting factors. To determine the relative influence of these properties, two notional alloys based on INCONEL X-750 are examined. The first, designated 750T^*, probes the effect of extending the

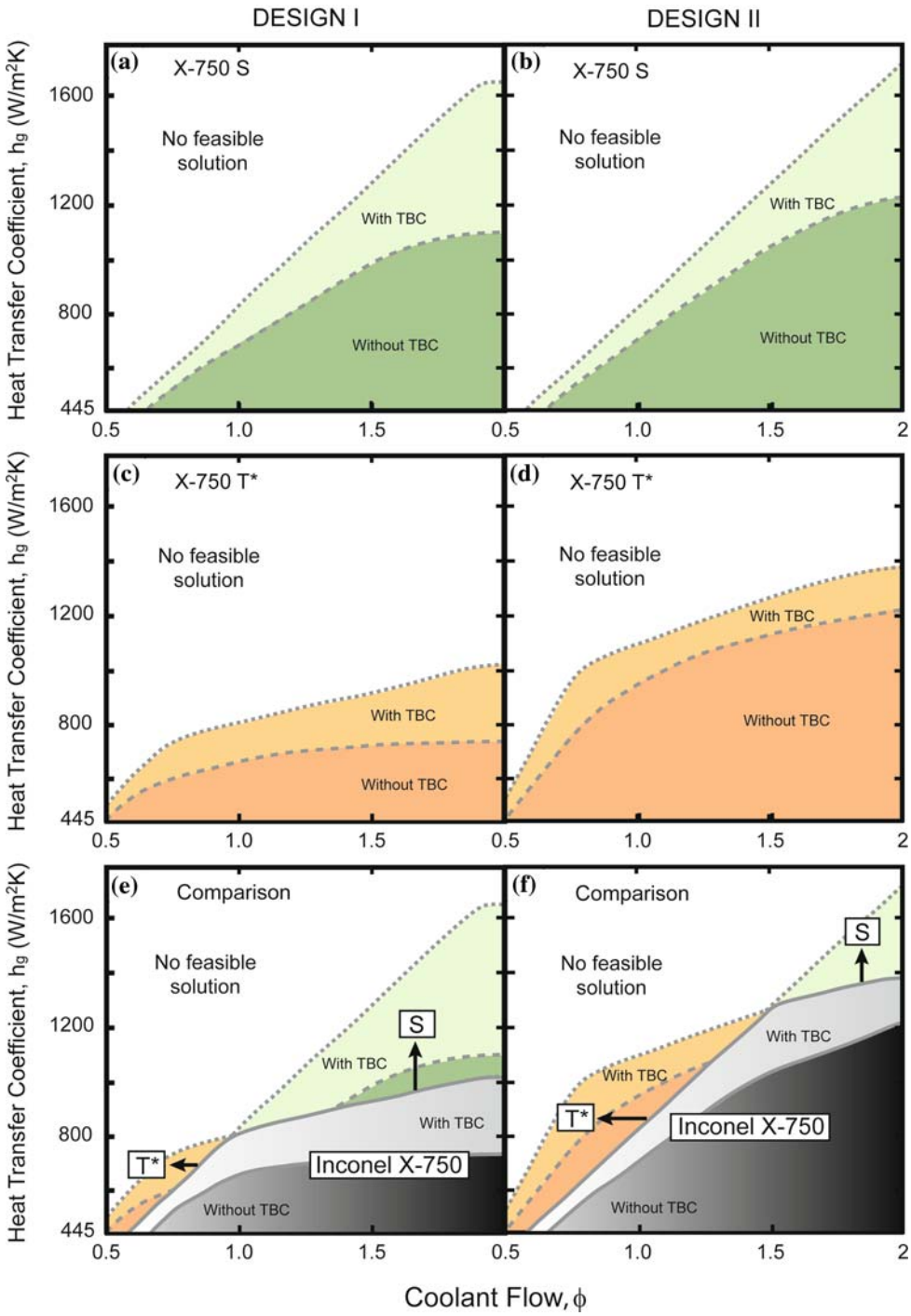

Fig. 9—Reclaimed feasibility space provided by two notional materials based on INCONEL X-750 (Figure 3) are displayed for both support designs. The first notional material 750*S*, designated *S*, examines the effect of elevating the yield strength at intermediate temperatures by 25 pct, analysis is shown both with (light green) and without (dark green) a TBC (*a* and *b*). The second notional material 750*T**, designated *T**, probes the effect of extending the maximum use temperature by 25 pct; again both with (light orange) and without (dark orange) a TBC (*c* and *d*). For comparison, the notional results are superimposed on the original performance maps for INCONEL X-750 (*e* and *f*).

maximum use temperature by 25 pct (all other properties and parameters kept the same). The second, designated 750*S*, examines the effect of elevating the yield strength at intermediate temperatures by 25 pct. The ensuing performance maps are presented in Figures 9(a) through (e). In general, the alloys 750*T** and 750*S* extend the area of feasibility in the directions of lower flow rates and higher heat transfer, respectively. While these benefits seem qualitatively self-evident, the specific merits only emerge upon utilizing the code. Alloy 750*T** improves the viability at the lowest flow rates provided that the heat transfer remains low. It does

not reduce the weight for thermal circumstances wherein optimal solutions already exist for INCONEL X-750 (Figures 10(a) through (d)). By contrast, 750*S* substantially reduces the weight within the existing operational domain (Figures 10(a) through (d)), but can only extend the feasibility to greater heat transfer when the fuel flow rates are intermediate to high (Figures 9(a), (b), (e), and (f)). More comprehensive assessments could be made by superimposing the thermal conditions and constraints accompanying an expected flight corridor onto the maps. For example, if the flight imposes a restriction on coolant flow $\phi \leq 1$, pursuing alloy X-750*T** would be preferable.

VI. CONCLUDING REMARKS

A procedure has been presented for ascertaining performance-limiting properties of candidate materials for actively cooled panels subject to combined thermal and pressure loads. The method has been illustrated for a propulsion system applicable to Mach 7 flight operations. Feasibility domains have been determined as functions of the coolant flow rate and heat transfer and materials that provide solutions at lowest weight identified. The assessment highlights the nonlinear relationships between feasibility, weight, and the salient material properties, especially the high temperature limit and the intermediate temperature strength. An example has been presented to demonstrate the specific benefits of next-generation alloys for weight reduction and design space reclamation. Moreover, a direct connection has been made between lower coolant flow rate operations and the softening temperature of the material.

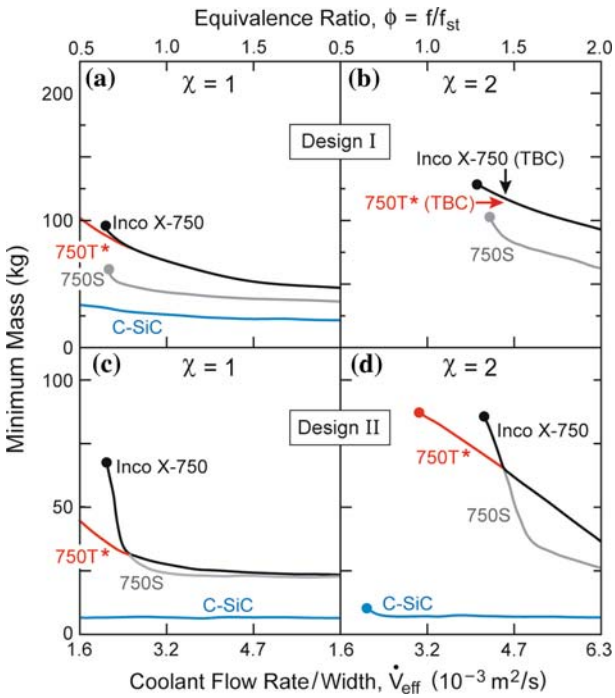

Fig. 10—Weight-performance charts illustrate the relative weight savings achieved by the notional materials for Designs I and II. The charts examine performance with two levels of fixed combustion heat transfer $\chi = 1$ and $\chi = 2$. Note that for $\chi = 2$ and Design I, INCONEL X-750 and 750*T** require a TBC, whereas 750*S* survives without a TBC. All other materials shown are absent a TBC. Results for 750*S* and 750*T** are not shown where they coincide with those for 750. Note the difference in scale on the minimum mass ordinate that results from the difference in design support condition.

ACKNOWLEDGMENTS

This work was supported by the ONR through a MURI program on Revolutionary Materials for Hypersonic Flight (Contract No. N00014-05-1-0439). The authors are thankful to David Marshall, Teledyne, and Thomas A. Jackson, Daniel J. Risha, and William M. Roquemore, AFRL, for insightful discussions.

APPENDIX I: SYNOPSIS OF THE CODE

The protocol employed for thermostructural analysis and design optimization consists of the following steps (Figure A1). (1) A range is defined for the expected heating loads (represented by the heat-transfer coefficient h_G of the hot gases) and the cooling capability (represented by the coolant flow rate per unit width of panel $\dot{V}^{\text{eff}}$). (2) A material is selected with the property profile indicated in Table I. (3) At each point in $(h_G, \dot{V}^{\text{eff}})$ space, the design parameters are systematically varied over a prescribed range and the temperatures and stresses calculated for each combination. Upon comparison with material and coolant properties, the viability of the design is ascertained. (4) If provided

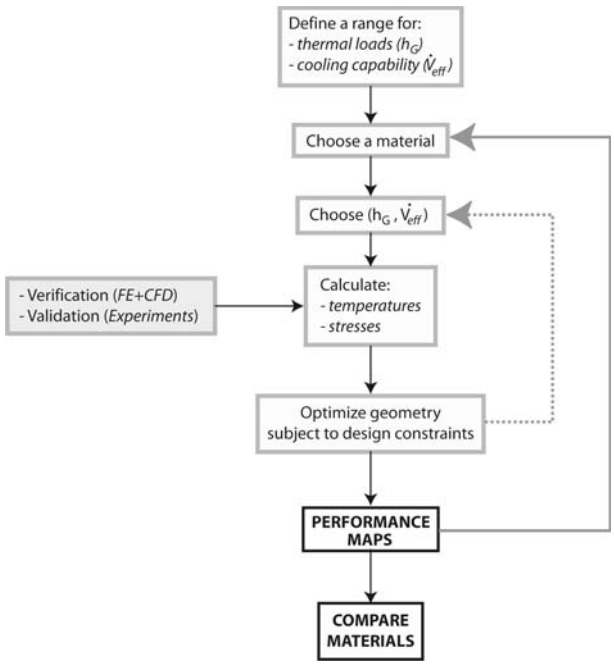

Fig. A1—Schematic of the materials selection procedure.

solutions exist, the design is optimized** for minimum mass, subject to a number of design constraints. Otherwise, if a solution is not found, the point $(h_G,\ \dot{V}^{\text{eff}})$ is deemed external to the design space. (5) Once the entire design space has been scanned† for each candidate material, comparisons are made of materials on the basis of structural robustness (namely, the extent of feasible solution area in $(h_G,\ \dot{V}^{\text{eff}})$ space) and weight efficiency.

**Numerical optimizations were performed using the quadratic optimizer MINCON in MATLAB (The MathWorks, Inc., Natick, MA). Several randomly generated initial guesses were used to escape local minima. In some cases, a manual optimization scheme was employed to verify the accuracy of the numerical results.

†A grid of 20 by 20 points was used to create these figures.

A. *Analytical Model for the Temperature Distributions*

Analytical expressions for the temperatures at critical locations in the panel are obtained *via* a thermal network approach, subject to four simplifying assumptions: (1) the adiabatic wall temperature T_{aw} and the heat-transfer coefficient h_G are uniform on the hot face; (2) the rest of the panel is thermally insulated, whereby all the heat is removed by forced convection in the cooling channels; (3) longitudinal conduction is negligible in the panel; and (4) the mixing-cup temperature T_f is used to model the coolant, hence neglecting cross-sectional variations in fluid temperature.

Based on the thermal network in Figure A2, the temperature in the fluid is

$$T_f = T_{aw} - \left(T_{aw} - T_f^0\right)\cdot\exp(-\beta z) \qquad [A1]$$

and the temperature distributions at the 18 locations depicted in Figure A3 are

$$T^{(i)} = T_{aw} - \left(T_{aw} - T_f^0\right)\cdot F^{(i)}\exp(-\beta z) \qquad [A2]$$

where $F^{(i)}$ and β depend on (Reference 1 for details): geometry of the panel (W, L, t_f, t_c); thermal conductivity of the material k_s; thermal properties of the coolant (thermal conductivity k_f; kinematic viscosity v_f; volumetric specific heat $\rho_f c_{p,f}$); prescribed heat-transfer coefficient on the hot side h_G; and prescribed volumetric flow rate $\dot{V}_{\text{eff}}$. Importantly, these functional dependencies are intertwined, thus precluding straightforward interpretation of the effect of each quantity on the temperature distribution.

The thermal stresses in the panel depend on two temperature differences: (1) across the top face $\Delta T_{\text{face}}(z)$ and (2) between the two faces $\Delta T_{\text{panel}}(z)$. For the sake of simplicity, these differences are averaged in the x direction, and can be expressed as

$$\begin{aligned}\Delta T_{face}(z) &= \left(T_{aw} - T_f^0\right)\cdot G_1\cdot\exp(-\beta z)\\ \Delta T_{panel}(z) &= \left(T_{aw} - T_f^0\right)\cdot G_2\cdot\exp(-\beta z)\end{aligned} \qquad [A3]$$

where G_1 and G_2 depend on the same quantities as $F^{(i)}$.

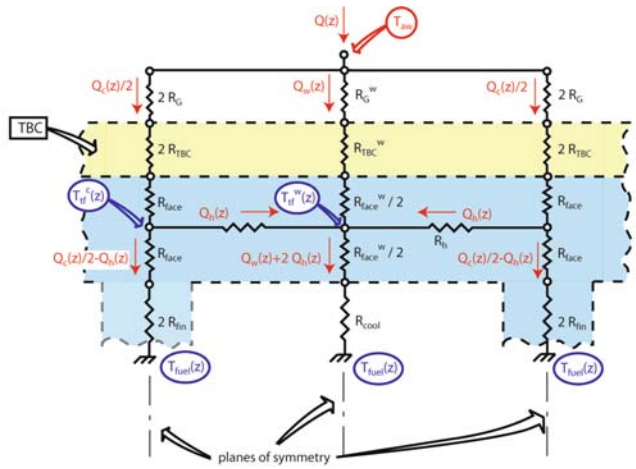

OVER THE WEB	$R_G = \frac{1}{h_G\, t_c}$	$R_{TBC} = \frac{t_{TBC}}{k^{\perp}_{TBC}\, t_c}$	$R_{face} = \frac{t_f}{k^{\perp}_s\, t_c}$	$R_{fin} = \frac{\tanh^{-1}\sqrt{2h_c/k^{\parallel}_s t_c}\, L}{\sqrt{2h_c/k^{\parallel}_s t_c}\, k^{\parallel}_s t_c}$	$R_h = \frac{W\ \ t_c/2}{4\, k^{\parallel}_s t_f}$
BETWEEN WEBS	$R^w_G = \frac{t_c}{W} R_G$	$R^w_{TBC} = \frac{t_c}{W} R_{TBC}$	$R^w_{face} = \frac{t_c}{W} R_{face}$	$R_{cool} = \frac{1}{h_c\, W}$	

Fig. A2—Thermal resistance network used to determine temperature distributions, along with expressions for all relevant thermal resistances.

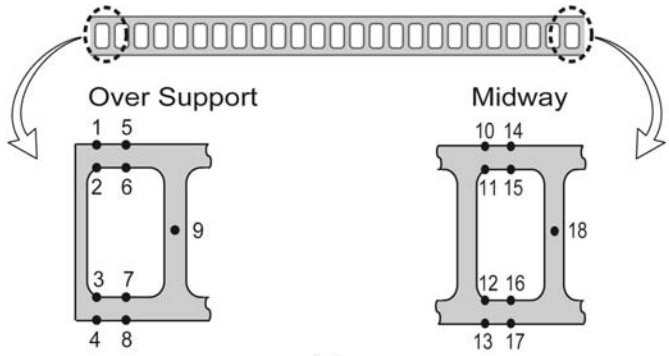

(a)

Sign of Component Stresses in the Channel Over the Supports

Points in Panel	ΔT panel	ΔT face	P cool	P comb
1	-	-	-	+
2	-	+	+	+
3	+	n/a	+	-
4	+	n/a	-	-
5	-	-	+	+
6	-	+	-	+
7	+	n/a	-	-
8	+	n/a	+	-
9	n/a	n/a	+	n/a

(b)

Sign of Component Stresses in the Channel Midway Between Supports

Points in Panel	ΔT panel	ΔT face	P cool	P comb
10	-	-	-	-
11	-	+	+	-
12	+	n/a	+	+
13	+	n/a	-	+
14	-	-	+	-
15	-	+	-	-
16	+	n/a	-	+
17	+	n/a	+	+
18	n/a	n/a	+	n/a

(c)

Fig. A3—(*a*) Unit cells susceptible to local yielding and the 18 critical points. A catalogue of the signs of component stresses for points within the unit cell (*b*) over a support and (*c*) between supports. The possible contributions to stress are thermally and mechanically induced by ΔT_{panel}, ΔT_{face}, p_{cool}, and p_{comb}. Note ΔT_{panel} and ΔT_{face} are the relevant temperature differences across the panel and top face, respectively. Figure 1 indicates the mechanical pressure loads p_{cool} and p_{comb}. Compression (−) and tension (+) are listed when applicable for Design I. All possible contributions to stress reinforce only for point 10.

The accuracy of this analytical model was verified with a number of selected computational fluid dynamics and finite element simulations; the temperature distribution was captured by Eq. [2] to within ~1 pct and the temperature gradients were captured by Eq. [3] to within ~8 pct.[1]

B. *Analytical Model for Stress Distributions in the Panel*

Stresses are induced in the panel by mechanical phenomena (combustion chamber pressure p_{comb} and coolant pressure p_{cool}) and thermal phenomena (ΔT_{tf} and ΔT_{panel}). Assuming generalized plane strain conditions (no rotation about the x and y axes), the mechanical stresses (membrane + bending) at any of the 18 locations depicted in Figure A3 are given by

$$\sigma_{m,x}^{(i)} = A^{(i)} p_{\text{cool}} + B^{(i)} p_{\text{comb}}$$
$$\sigma_{m,z}^{(i)} = \nu\, \sigma_{m,x}^{(i)} \qquad [A4]$$

where the functions $A^{(i)}$ and $B^{(i)}$ depend on the panel geometry and the design scenario (Figure 2, details in Reference 1) and ν is the Poisson's ratio of the material.

Similarly, the thermal stresses can be expressed as

$$\sigma_{T,x}^{(i)} = \frac{E\alpha}{(1-\nu)}\left(C_x^{(i)}\, \Delta T_{\text{face}}^{(i)} + D_x^{(i)}\, \Delta T_{\text{panel}}^{(i)}\right)$$
$$\sigma_{T,z}^{(i)} = \frac{E\alpha}{(1-\nu)}\left(C_z^{(i)}\, \Delta T_{\text{face}}^{(i)} + D_z^{(i)}\, \Delta T_{\text{panel}}^{(i)}\right) \qquad [A5]$$

with E and α the Young's modulus and the coefficient of thermal expansion of the material, respectively. The quantities $C_x^{(i)}$, $D_x^{(i)}$, $C_z^{(i)}$, and $D_z^{(i)}$ are a function of geometry only (different expressions pertain to the x and z stresses because of the anisotropy of the core). Reference 1 provides details.

The signs of the various stress contributions at the 18 critical locations are catalogued in Figure A3 for both

design scenarios. The accuracy of this analytical model was verified with a number of selected finite element simulations; the stress distribution was captured to within ~10 pct at the top face and ~20 pct at the bottom face.[1] The internal corners exhibit stress intensifications and the agreement is somewhat worse. In reality, localized plastic deformation will ameliorate the stress concentration.

APPENDIX II: ACTIVITY INDICES

For any choice of input parameters (h_G and $\dot{V}_{\text{eff}}$), a quadratic optimizer is invoked to select the geometry that minimizes the weight of the panel while meeting all the prescribed design constraints. Temperature and stress distributions are calculated with the methodology described in Appendix I and listed in Table III. This appendix describes the nature of the applied constraints, dividing them in three groups: group I includes constraints that enforce the resistance of the panel under the prescribed thermal and mechanical loads; group II includes system-imposed constraints (on coolant temperature and allowable pressure drop); and group III contains design and manufacturing constraints (minimum gages).

A. *Group I Constraints*

1. *(1–3) Yielding or Fracture*‡

‡The von Mises yielding criterion is used for metallic candidates. For CMCs, a maximum principal stress criterion is used in Ref. 1.

For metals failure is defined as the onset of yielding. The Von Mises criterion is used. Under the simultaneous action of thermal and mechanical loads (Appendix I), the Von Mises stress at any critical location (i) is given by

$$\sigma^{(i)}_{VM,\text{comb}} = \frac{1}{2}\left[\left(\sigma^{(i)}_{m,x} + \sigma^{(i)}_{T,x} - \sigma^{(i)}_{m,z} - \sigma^{(i)}_{T,z}\right)^2 + \left(\sigma^{(i)}_{m,x} + \sigma^{(i)}_{T,x}\right)^2 + \left(\sigma^{(i)}_{m,z} + \sigma^{(i)}_{T,z}\right)^2\right] \quad [B1]$$

with the stress components given by Eqs. [4] and [5].

The temperature of the solid at each of these 18 critical locations (Eq. [2]) is used to identify the associated (temperature-dependent) yield strength, modeled as linearly decreasing when $T^{(i)} < T^*$, with T^* the softening temperature of the alloy (Table I).[1]

The constraint can then be expressed as: $\max_{i=1-18}\left\{\sigma^{(i)}_{VM,\text{comb}}/\sigma_{\text{yield}}(T^{(i)})\right\} \le 1$. The constraint activity is monitored through the ratio

$$\Pi^{(1)} = \max_{i=1-18}\left\{\sigma^{(i)}_{VM,\text{comb}}\Big/\sigma_{\text{yield}}(T^{(i)})\right\} \quad [B2a]$$

To avert yielding, it is insufficient to restrict only the combined stresses because the thermal and mechanical stresses may have opposite signs in some locations (Figure A3). Two more constraints must be imposed, one for mechanical stresses ($\sigma^{(i)}_{VM,\text{mech}}$) and the other for thermal stresses ($\sigma^{(i)}_{VM,\text{therm}}$). The resulting constraint activity indices are

$$\Pi^{(2)} = \max_{i=1-18}\left\{\sigma^{(i)}_{VM,\text{mech}}\Big/\sigma_{\text{yield}}(T^{(i)})\right\} \quad [B2b]$$

$$\Pi^{(3)} = \max_{i=1-18}\left\{\sigma^{(i)}_{VM,\text{therm}}\Big/\sigma_{\text{yield}}(T^{(i)})\right\} \quad [B2c]$$

Well-designed CMCs typically fail when the normal stress along the primary fiber orientation attains either the ultimate tensile strength or the compressive strength. Assuming for simplicity that the strengths in tension and compression are identical and temperature independent (reasonable for SiC/SiC and C/SiC),[13,14] the ensuing constraint is

$$\max_{i=1\div18}\left\{\max\left\{\frac{\left|\sigma^{(i)}_{m,x} + \sigma^{(i)}_{T,x}\right|}{\sigma_{\text{ult}}}, \frac{\left|\sigma^{(i)}_{m,z} + \sigma^{(i)}_{T,z}\right|}{\sigma_{\text{ult}}}\right\}\right\} \le 1 \quad [B3]$$

where the ultimate strength σ_{ult} is assumed temperature independent. Activity indices analogous to Eqs. [7] through [9] arise.

2. *(4) Material softening*

The maximum temperature in the panel, found at the exit (Eq. [2]), must remain below the material softening limit T^*. Above this limiting temperature, the load-bearing capacity decreases dramatically. The constraint can be expressed as: $T^{\max}_{\text{solid}} \le T^*$. The constraint activity is monitored through the ratio

$$\Pi^{(4)} = \frac{T^{\max}_{\text{solid}}}{T^*} \quad [B4]$$

B. *Group II Constraints*

1. *(5) Fuel coking*

The maximum temperature in the fuel, taken at the exit (Eq. [1]), must remain below the coking temperature (Table II). At the coking temperature, the hydrocarbon fuel undergoes chemical reactions causing deposition of carbon and fouling of the heat-transfer surfaces.[15] The constraint can be expressed as $T^{\max}_{\text{fuel}} = T_{\text{fuel}}(Z) \le T_{\text{coke}}$. The constraint activity is monitored through the ratio

$$\Pi^{(5)} = \frac{T^{\max}_{\text{fuel}}}{T_{\text{coke}}} \quad [B5]$$

2. *(6) Pressure drop*

A pressure drop Δp is caused by viscous dissipation and other losses in the cooling channels. The Δp is quantified through a correlation for the friction factor.[16] Pressure losses at the manifold/panel connections are neglected. To minimize requirements on pumping

power, the maximum allowable pressure drop (over a 2-m combustor length) is taken as $\Delta p^c \approx 0.1$ MPa. The constraint is then simply $\Delta p \le \Delta p^c$. The constraint activity is monitored through the ratio

$$\Pi^{(6)} = \frac{\Delta p}{\Delta p^c} \qquad [B6]$$

C. *Group III Constraints*

The remaining constraints refer to the allowable range of the geometric variables to be optimized, depicted in Figure 1. These are as follows.

1. *(7) TBC thickness*

The presence of a TBC can be enabling in some cases. It functions by decreasing the maximum temperature in the solid. To avoid unnecessary costs, the optimizer will only add a coating if the thermal benefit will allow a lower-weight solution. In practice, in high heat flux situations, TBCs can be deposited to a maximum thickness of ≈0.3 mm without spalling.[17] Additionally, the TBC must be significantly thinner than the substrate $t_{\mathrm{TBC}} \le 0.25 t_f$. The ensuing dimensional constraint for the TBC layer is $t_{\mathrm{TBC}} \le t_{\mathrm{TBC}}^{\max}$, where $t_{\mathrm{TBC}}^{\max} = \min\{0.25 t_f, 0.3\,\mathrm{mm}\}$. The constraint activity is monitored through the ratio

$$\Pi^{(7)} = \frac{t_{\mathrm{TBC}}}{t_{\mathrm{TBC}}^{\max}} \qquad [B7]$$

2. *(8–11) Additional constraints on dimensions*

Additional constraints are imposed on the dimensions L, W, t_f, and t_c (Table III), resulting in four more activity indices.

NOMENCLATURE

$A^{(i)}$, $B^{(i)}$	nondimensional functions
$C_x^{(i)}$, $C_z^{(i)}$	nondimensional functions
$c_{p,f}$	specific heat of the coolant (J/kg K)
$D_x^{(i)}$, $D_z^{(i)}$	nondimensional functions
E	Young's modulus (Pa)
f	fuel/air mass ratio
f_{st}	stoichiometric fuel/air mass ratio
$F^{(i)}$	nondimensional function
G_1, G_2	nondimensional functions
h_G	heat-transfer coefficient on the combustor side (W/m^2 K)
h_G^{nom}	nominal combustion heat-transfer coefficient for a Mach 7 vehicle (W/m^2 K)
k_s	thermal conductivity of the material (W/m K)
k_f	thermal conductivity of the coolant (W/m K)
L	height of cooling channel (m)
p_{cool}	pressure in the coolant (Pa)
p_{comb}	pressure in the combustion chamber (Pa)
s	trajectory denoting the border of feasible design space
T_{aw}	adiabatic wall temperature in the combustion chamber
T_{coke}	coking temperature of the coolant (K)
T_f	coolant temperature (K)
T_f^0	coolant entry temperature (K)
$T_{\mathrm{fuel}}^{\max}$	maximum coolant temperature (K)
$T_{\mathrm{solid}}^{\max}$	maximum temperature in the material (K)
$T^{(i)}$	temperature at location (i) in the material (K)
T^*	maximum allowable temperature in the material (K)
t_c	core web thickness (m)
t_f	face sheet thickness (m)
t_{TBC}	thickness of TBC (m)
$\dot{V}_{\mathrm{eff}}$	volumetric fuel flow rate per unit width scaled by combustor area ratio (m^2/s)
W	width of cooling channel (m)
Z	panel length (m)
Δp	viscous pressure drop across the panel (Pa)
Δp^c	critical pressure drop (Pa)
α	coefficient of thermal expansion of the material (K^{-1})
β	inverse length constant in the temperature distribution (1/m)
χ	nondimensional heat-transfer coefficient for combustion (h_G/h_G^{nom})
ϕ	equivalence ratio (f/f_{st})
ν_f	kinematic viscosity of the coolant (m^2/s)
ν	Poisson's ratio of the material
$\prod$	nondimensional constraint activity index
ρ_f	mass density of the coolant (kg/m^3)
σ_{ult}	critical strength of a CMC material (MPa)
σ_{yield}	yield strength of a metallic material (MPa)
$\sigma_{VM,\mathrm{comb}}^{(i)}$	von Mises stress due to combined thermal/mechanical loads at location (i) (MPa)
$\sigma_{VM,\mathrm{mech}}^{(i)}$	von Mises stress due to mechanical loads at location (i) (MPa)
$\sigma_{VM,\mathrm{therm}}^{(i)}$	von Mises stress due to thermal loads at location (i) (MPa)
$\sigma_{m,x}^{(i)}$	mechanical stress at location i along the x direction (Pa)
$\sigma_{m,z}^{(i)}$	mechanical stress at location i along the z direction (Pa)
$\sigma_{T,x}^{(i)}$	thermal stress at location i along the x direction (Pa)
$\sigma_{T,z}^{(i)}$	thermal stress at location i along the z direction (Pa)

REFERENCES

1. L. Valdevit, N. Vermaak, F.W. Zok, and A.G. Evans: *J. Appl. Mech.*, 2008, vol. 75 (6), pp. 61022–37.
2. L. Valdevit, N. Vermaak, K. Hsu, F.W. Zok, and A.G. Evans: *AIAA Conf.*, Canberra, Australia, 2006.
3. A.G. Evans, D.R. Clarke, and C.G. Levi: *J. Eur. Ceram. Soc.*, 2008, vol. 28, pp. 1405–19.
4. D.J. Risha and T.A. Jackson (AFRL/RZA): personal communication.
5. W.J. Mills: *Metall. Trans. A*, 1980, vol. 11A, pp. 1039–47.
6. M.C. Pandey, D.M.R. Taplin, and A.K. Mukherjee: *Metall. Trans. A*, 1984, vol. 15A, pp. 1763–67.

7. S.J. Johnson, B. Tryon, and T.M. Pollock: *Acta Mater*., 2008, vol. 56, pp. 4577–84.
8. J.M. Larsen, S.M. Russ, and J.W. Jones: *Metall. Mater. Trans. A*, 1995, vol. 26A, pp. 3211–23.
9. B.P. Bewlay, M.R. Jackson, J.C. Zhao, and P.R. Subramanian: *Metall. Mater. Trans. A*, 2003, vol. 34A, pp. 2043–52.
10. M.D. Novak and C.G. Levi: *Proc. ASME IMECE*, Seattle, WA, Nov. 11–15, 2007.
11. P.R. Chandra, C.R. Alexander, and J.C. Han: *Int. J. Heat Mass Transfer*, 2003, vol. 46, pp. 481–95.
12. R.L. Webb, E.R.G. Eckert, and R.J. Goldstein: *Int. J. Heat Mass Transfer*, 1972, vol. 15, pp. 180–84.
13. M.D. Wang and C. Laird: *Acta Mater*., 1996, vol. 44 (4), pp. 1371–87.
14. M.D. Wang and C. Laird: *J. Mater. Sci*., 1996, vol. 31 (8), pp. 2065–69.
15. L.J. Spadaccini: *J. Eng. Gas Turbines Power*, 2001, vol. 123 (4), pp. 741–46.
16. A. Bejan: *Convection Heat Transfer*, Wiley, Hoboken, NJ, 2004, pp. 384–404.
17. A.G. Evans and J.W. Hutchinson: *Surf. Coat. Technol*., 2007, vol. 201, pp. 7905–16.